

Unveiling the $K_1(1270)$ double-pole structure in the $\bar{B} \rightarrow J/\psi \rho \bar{K}$ and $\bar{B} \rightarrow J/\psi \bar{K}^* \pi$ decays

J. M. Dias,^{*} G. Toledo,^{1,†} L. Roca,^{2,‡} and E. Oset^{3,§}

¹*Instituto de Física, Universidad Nacional Autónoma de México,
AP 20-364, Ciudad de México 01000, Mexico.*

²*Departamento de Física, Universidad de Murcia, E-30100 Murcia, Spain.*

³*Departamento de Física Teórica and IFIC,
Centro Mixto Universidad de Valencia-CSIC,
Institutos de Investigación de Paterna,
Aptdo. 22085, 46071 Valencia, Spain.*

Abstract

By looking at the pseudoscalar-vector meson spectra in the $\bar{B} \rightarrow J/\psi \rho \bar{K}$ and $\bar{B} \rightarrow J/\psi \bar{K}^* \pi$ weak decays, we theoretically investigate the double-pole structure of the $K_1(1270)$ resonance by using the Chiral Unitary approach to account for the final state interactions between the pseudoscalar and vector mesons. The $K_1(1270)$ resonance appears as dynamically generated through these interactions in coupled channels and influence the shape of the invariant mass distributions under consideration. We show how those shapes are affected by the $K_1(1270)$ double-pole structure to confront the results from our model with future experiments that might investigate the PV spectra in these decays.

^{*} jorgivan.mdias@gmail.com

[†] toledo@fisica.unam.mx

[‡] luisroca@um.es

[§] Eulogio.Oset@ific.uv.es

I. INTRODUCTION

The observation of the axial vector mesons $K_1(1270)$ and $K_1(1400)$ [1, 2] pointed them to be identified as the expected 1^+ strange mesons from the quark model. Subsequent experiments have explored their properties and decay modes [3]. While the $K_1(1270)$ can be identified as dominated by a $K\rho$ decay channel, the $K_1(1400)$ is observed to decay mostly through the $K^*(892)\pi$ one. These states have been studied in terms of the mixing of the interaction states and their corresponding decay modes (see for example [4–6]). An exhaustive analysis of the 1^+ low lying mesons as dynamically generated resonances, found that the $S = 1$ and $I = 1/2$ poles were not compatible with the above assignment but rather identified as a double pole structure around the $K_1(1270)$ [7]. This result triggered studies looking for scenarios where this prediction can be tested. A data based analysis [8] provided additional support to the existence of two states, one with a mass of 1195 MeV, coupling mostly to the $K^*(892)\pi$ channel and the other with a mass of 1284 MeV to the $K\rho$ channel. It has been proposed a set of reactions to observe these two states, for example the $D^0 \rightarrow \pi^+VP$ [9], which is similar to $B^- \rightarrow J/\psi K_1^-(1270)$, with the hadronization involving three light mesons. More recently, another possibility considered the $D^+ \rightarrow \nu l^+ K_1(1270)$ decay [10], identifying the signatures in the invariant mass distributions of the decaying $K_1(1270)$. On the other hand, expected improvements on the experimental capabilities to study B mesons decays with higher statistics, like in Belle II experiment, make this an interesting scenario to look for.

In this work we provide an additional possibility, considering decays of the form $\bar{B}^0 \rightarrow J/\psi VP$, where VP are the Vector and Pseudoscalar meson pairs, $\bar{K}\rho$ and $\bar{K}^*\pi$, using the chiral unitary approach, and looking for signatures of the two $K_1(1270)$ states. In section II, we present the formalism for the elementary production at the quark level where the different VP channels are related by $SU(3)$ arguments. Then we account for the final VP interaction implementing meson-meson scattering based on the Chiral Unitary approach. In section III we compute the invariant mass distribution for the VP pair and its structure in terms of the individual poles, and identify the regions where the signature of such poles can be extracted.

II. FORMALISM

A. The PV pseudoscalar and vector mesons production

The relevant contribution for the $\bar{B} \rightarrow J/\psi PV$ reaction is given by the diagram at the quark level illustrated in Fig. 1. It starts with a $b\bar{d}$ quark pair, forming the initial \bar{B}^0 meson,

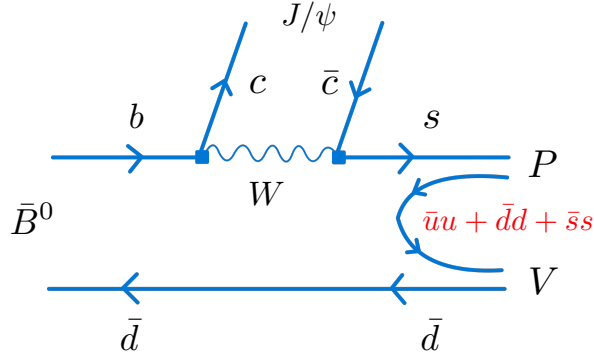


FIG. 1. Dominant diagram for the $\bar{B} \rightarrow J/\psi(PV)$ reaction at the quark level. In the first step, a b quark decays into a c one by emission of a gauge boson W which, then coalesce into a strange quark s along with \bar{c} one. Finally, we are left with a $c\bar{c}$ pair, forming the J/ψ , and the $s\bar{d}$ one, where this latter pair is hadronized in order to produce a pseudoscalar-vector meson pair emerging as final state.

in which the b quark converts into a c one by emitting a W boson, that later on coalesce into an anti charm \bar{c} along with a strange quark s . In the end, we are left with a $c\bar{c}$ pair making up a J/ψ meson, considered as a spectator, and a $s\bar{d}$ pair. In order to produce a pseudoscalar as well as a vector meson, a $\bar{q}q$ pair with the quantum numbers of the vacuum is added to the already existing $s\bar{d}$ pair, according to the 3P_0 model [11–13]. Therefore, the final meson-meson hadronic state will have the following quark flavor combination:

$$|H\rangle = |s(\bar{u}u + \bar{d}d + \bar{s}s)\bar{d}\rangle. \quad (1)$$

However, Eq. (1) above only refers to the quark content for the final mesonic states and it does not carry out any information about the pseudoscalar or vector nature of those hadronic

states. This is done by defining the $q\bar{q}$ -matrix, denoted as M , written as

$$M = \begin{pmatrix} u\bar{u} & u\bar{d} & u\bar{s} \\ d\bar{u} & d\bar{d} & d\bar{s} \\ s\bar{u} & s\bar{d} & s\bar{s} \end{pmatrix}, \quad (2)$$

so that its link to Eq. (1) provides

$$|H\rangle = |s(\bar{u}u + \bar{d}d + \bar{s}s)\bar{d}\rangle = \sum_i |s\bar{q}_i q_i \bar{d}\rangle = |M_{3i} M_{i2}\rangle = |(MM)_{32}\rangle. \quad (3)$$

The final meson-meson components are found by establishing the correspondence between M and the pseudoscalar and vector meson matrices, that is

$$M \Rightarrow P = \begin{pmatrix} \frac{\pi^0}{\sqrt{2}} + \frac{\eta}{\sqrt{3}} + \frac{\eta'}{\sqrt{6}} & \pi^+ & K^+ \\ \pi^- & -\frac{\pi^0}{\sqrt{2}} + \frac{\eta}{\sqrt{3}} + \frac{\eta'}{\sqrt{6}} & K^0 \\ K^- & \bar{K}^0 & -\frac{1}{\sqrt{3}}\eta + \sqrt{\frac{2}{3}}\eta' \end{pmatrix}, \quad (4)$$

and

$$M \Rightarrow V = \begin{pmatrix} \frac{\rho^0}{\sqrt{2}} + \frac{\omega}{\sqrt{2}} & \rho^+ & K^{*+} \\ \rho^- & -\frac{\rho^0}{\sqrt{2}} + \frac{\omega}{\sqrt{2}} & K^{*0} \\ K^{*-} & \bar{K}^{*0} & \phi \end{pmatrix}, \quad (5)$$

where the standard $\eta - \eta'$ [14] and $\omega_1 - \omega_8$ mixings have been used for P and V , respectively, in order to match the right flavor content of the matrix M .

Since we aim at describing a reaction with a pseudoscalar along with a vector meson as final states, the matrix M in Eqs. (4) and (5) should combine to itself according to Eq. (3) in such a way that it gives the product PV or VP . There is nothing in our model that privileges one against the other, then we consider an equal-weighted combination between them in Eq. (3) so that it can be rewritten as

$$|H\rangle = |(PV)_{32}\rangle + |(VP)_{32}\rangle. \quad (6)$$

Therefore, the pseudoscalar and the vector mesons produced in the reaction are

$$|H\rangle = |\rho^+ \bar{K}^-\rangle - \frac{1}{\sqrt{2}}|\rho^0 \bar{K}^0\rangle + |K^{*-} \pi^+\rangle - \frac{1}{\sqrt{2}}|\bar{K}^{*0} \pi^0\rangle + \frac{1}{\sqrt{2}}|\omega \bar{K}^0\rangle + |\phi \bar{K}^0\rangle, \quad (7)$$

where a term corresponding to the $\bar{K}^{*0}\eta$ channel has canceled out in the evaluation of Eq. (6) by using Eqs. (4) and (5). Note that the procedure adopted provides the final PV meson-meson components as well as their relative weights, which will play a significant role in the mass spectrum.

The final $|H\rangle$ state can be written in the isospin basis considering the following multiplets: $(-\rho^+, \rho^0, \rho^-)$, $(\bar{K}^0, -K^-)$, $(-\pi^+, \pi^0, \pi^-)$ for the ρ , \bar{K} and π mesons, respectively. Then, the final PV states in the isospin $I = 1/2$ are given by

$$\begin{aligned} |\rho \bar{K}\rangle_{I_3=1/2}^{I=1/2} &= \sqrt{\frac{2}{3}} |\rho^+ K^- \rangle - \sqrt{\frac{1}{3}} |\rho^0 \bar{K}^0 \rangle, \\ |\bar{K}^* \pi\rangle_{I_3=1/2}^{I=1/2} &= -\sqrt{\frac{2}{3}} |K^{*-} \pi^+ \rangle + \sqrt{\frac{1}{3}} |\bar{K}^{*0} \pi^0 \rangle. \end{aligned} \quad (8)$$

Using this we can recast $|H\rangle$ as

$$|H\rangle = \sqrt{\frac{3}{2}} |\rho \bar{K}\rangle_{I_3=1/2}^{I=1/2} - \sqrt{\frac{3}{2}} |\bar{K}^* \pi\rangle_{I_3=1/2}^{I=1/2} + \frac{1}{\sqrt{2}} |\omega \bar{K}\rangle_{I_3=1/2}^{I=1/2} + |\phi \bar{K}\rangle_{I_3=1/2}^{I=1/2}. \quad (9)$$

This last equation also provides us the relative weights, denoted as h_i , in the isospin basis between the i -th PV channels above. They are

$$\begin{aligned} h_{\rho \bar{K}} &= \sqrt{\frac{3}{2}}; & h_{\bar{K}^* \pi} &= -\sqrt{\frac{3}{2}}; \\ h_{\omega \bar{K}} &= \frac{1}{\sqrt{2}}; & h_{\phi \bar{K}} &= 1. \end{aligned} \quad (10)$$

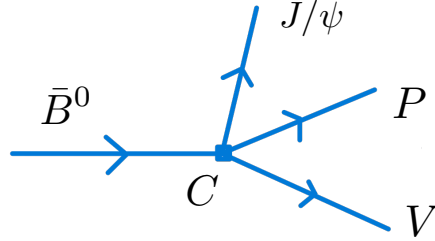


FIG. 2. Amplitude for the $\bar{B} \rightarrow J/\psi(PV)$ decay. The C constant is the parametrization of the weak vertex.

The differential decay width for the $\bar{B} \rightarrow J/\psi(PV)$ process, illustrated in Fig. 2 is given by

$$\frac{d\Gamma}{dM_{inv}} = \frac{1}{(2\pi)^3} \frac{1}{4M_B^2} p_{J/\psi} \tilde{p}_{\pi(\bar{K})} |T_{B \rightarrow J/\psi(PV)}|^2, \quad (11)$$

where M_B is the \bar{B} meson mass while $p_{J/\psi}$ and $\tilde{p}_{\pi(\bar{K})}$ are the momentum associated with J/ψ in the \bar{B} rest frame and $\pi(\bar{K})$ mesons in the PV rest frame, as a function of the invariant

mass M_{inv} ascribed to the PV pair, respectively, and M_{inv} , the invariant mass of the PV pair. They are

$$p_{J/\psi} = \frac{\lambda^{1/2}(M_B^2, M_{J/\psi}^2, M_{inv}^2)}{2M_B}, \quad (12)$$

$$\tilde{p}_{\bar{K}} = \frac{\lambda^{1/2}(M_{inv}^2, M_\rho^2, m_{\bar{K}}^2)}{2M_{inv}} \text{ for the } \rho\bar{K} \text{ channel}, \quad (13)$$

$$\tilde{p}_\pi = \frac{\lambda^{1/2}(M_{inv}^2, M_{\bar{K}^*}^2, m_\pi^2)}{2M_{inv}} \text{ for the } \bar{K}^*\pi \text{ channel}, \quad (14)$$

with λ standing for the well-known Källén function. The weak vertex is parametrized by a constant C which is built in the $T_{\bar{B} \rightarrow J/\psi(PV)}$ amplitude for the processes we are concerned with.

For the evaluation of the full decay amplitude, needed in Eq. (11), we have to consider the diagrams in Fig. 3, where the final state interaction mechanism is implemented to take into account the $K_1(1270)$ resonance contribution for the invariant mass spectra we are interested in. Since we are interested in the distributions with $\rho\bar{K}$ and $\bar{K}^*\pi$ as final PV states, we have

$$T_{B \rightarrow J/\psi \rho \bar{K}} = C (\vec{\epsilon}_\psi \cdot \vec{\epsilon}_\rho) \left(h_{\rho\bar{K}} + \sum_i h_i G_i(M_{inv}) t_{i \rightarrow \rho\bar{K}}^{I=1/2}(M_{inv}) \right), \quad (15)$$

and

$$T_{B \rightarrow J/\psi \bar{K}^* \pi} = C (\vec{\epsilon}_\psi \cdot \vec{\epsilon}_{\bar{K}^*}) \left(h_{\bar{K}^*\pi} + \sum_i h_i G_i(M_{inv}) t_{i \rightarrow \bar{K}^*\pi}^{I=1/2}(M_{inv}) \right), \quad (16)$$

where the index i , running from 1 to 4, stands for each possible channel involved in the loop. They are: $i = 1$ for $\phi\bar{K}$, $i = 2$ for $\omega\bar{K}$, $i = 3$ for $\rho\bar{K}$, $i = 4$ for $\bar{K}^*\pi$. These loops are represented by the $G_i(M_{inv})$ which is the G -loop function (given as a function of the invariant mass M_{inv}) which we shall discuss in the next section. The h_i 's are the relative weights in the isospin basis, defined in Eq. (10) above. Moreover, ϵ_ψ , ϵ_ρ , $\epsilon_{\bar{K}^*}$ are the polarization vectors for the J/ψ , ρ , and \bar{K}^* mesons, respectively.

Furthermore, the amplitudes $t_{i \rightarrow \rho\bar{K}}^{I=1/2}$ and $t_{i \rightarrow \bar{K}^*\pi}^{I=1/2}$ in Eqs. (15) and (16) are the two-body scattering amplitudes for all possible transitions from the i -th channel to $\rho\bar{K}$ (and to $\bar{K}^*\pi$), which in our approach encode the resonance $K_1(1270)$ as dynamically generated through these interactions [8], and are explained in the following subsection.

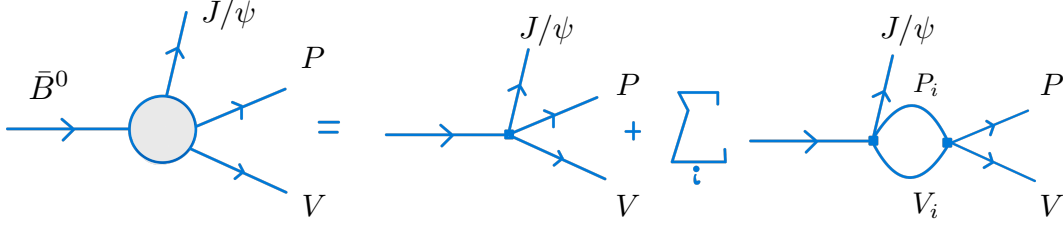


FIG. 3. Relevant diagrams contributing to the amplitude $T_{\bar{B} \rightarrow J/\psi(PV)}$. The first diagram on the right-hand side corresponds to the tree-level. On the other hand, the second one with a loop encodes the final state interaction mechanism and, actually it is a sum over all $P_i V_i$ pseudoscalar and vector mesons associated with the i -channel: $i = 1$ for $\phi \bar{K}$, $i = 2$ for $\omega \bar{K}$, $i = 3$ for $\rho \bar{K}$, $i = 4$ for $\bar{K}^* \pi$.

B. Final state interaction and the $K_1(1270)$ resonance

Once the final meson-meson pair is produced at tree-level in the $\bar{B} \rightarrow J/\psi PV$ reaction they undergo final state interaction from which the $K_1(1270)$ resonance emerges dynamically. In fact, in Ref. [8] this resonance is dynamically generated through the s -wave interaction between the pseudoscalar and vector mesons in the $I = 1/2$ channel. The final state interaction mechanism is introduced adopting a unitarization procedure using the Bethe-Salpeter equation in coupled channels, from which hadronic states show up as poles in the unphysical Riemann sheets of the scattering matrices. This approach is a unitary extension of the Chiral Perturbation theory, called Chiral Unitary approach[15–17], which has allowed to describe many hadronic resonances as composite states of mesons and/or baryons. In particular, in Ref. [8] the transition amplitudes $t_{i \rightarrow j}^{I=1/2}$ appearing in Eqs. (15) and (16) are unitarized by solving a coupled channel scattering equation in an algebraic form, written in matrix form as

$$t = (1 - V G)^{-1} V, \quad (17)$$

where in V_{ij} , t_{ij} the indices stand for the coupled channels: 1 for $\phi \bar{K}$, 2 for $\omega \bar{K}$, 3 for $\rho \bar{K}$, 4 for $\bar{K}^* \pi$ and 5 for $\bar{K}^* \eta$. In addition, V_{ij} is the interaction kernel which corresponds to the tree-level amplitudes evaluated for all channels we are considering in this work by using phenomenological Lagrangians (we refer the reader to Ref. [8] for more details about these

lagrangians). Furthermore, $G_k(s)$ is the meson-meson loop function associated to the k -th channel, which can be regularized either by dimensional or cutoff regularization schemes. In the present work, we follow Ref. [8] which has employed the former scheme. In this case, the $G_k(s)$ loop function is given by

$$G_k(\sqrt{s}) = \frac{1}{16\pi^2} \left\{ a(\mu) + \ln \frac{M_k^2}{\mu^2} + \frac{m_k^2 - M_k^2 + s}{2s} \ln \frac{m_k^2}{M_k^2} + \frac{q_k}{\sqrt{s}} [\ln(s - (M_k^2 - m_k^2) + 2q_k\sqrt{s}) + \ln(s + (M_k^2 - m_k^2) + 2q_k\sqrt{s}) - \ln(-s + (M_k^2 - m_k^2) + 2q_k\sqrt{s}) - \ln(-s - (M_k^2 - m_k^2) + 2q_k\sqrt{s})] \right\}, \quad (18)$$

where M_k and m_k stand for the vector and pseudoscalar meson masses in the k -th channel, respectively. Moreover, $a(\mu)$ is the subtraction constant and in this work we take $a(\mu) = -1.85$ for $\mu = 900$ MeV, which is the scale of dimensional regularization, obtained in Ref. [8] by fitting the experimental $K^-p \rightarrow K^- \pi^+ \pi^- p$ data. In addition, $q_k = |\vec{q}_k|$ is the on-shell three-momentum of the meson in the loop, given in the center of mass frame,

$$q_k = \frac{\lambda^{1/2}(s, M_k^2, m_k^2)}{2\sqrt{s}}. \quad (19)$$

The ρ and \bar{K}^* mesons have a relatively large width and hence a given mass distribution. In order to take this feature into account in our formalism, we convolve the loop function $G_k(s)$ with the corresponding vector meson spectral function

$$\text{Im}[D(s_V)] = \text{Im} \left(\frac{1}{s_V - M_V^2 + iM_V\Gamma_V} \right), \quad (20)$$

where M_V stands for the vector meson mass and Γ_V is the vector meson width, considered here as non-energy dependent. Choosing an energy-dependent form for Γ_V , as done in Refs. [9, 10], does not provide any significant change in our results compared with the usual uncertainties of our approach. The spectral function above is related to the exact propagator for the vector meson by using the Lehmann representation, which gives us

$$D(s) = -\frac{1}{\pi} \int_{s_{th}}^{\infty} ds_V \frac{\text{Im}[D(s_V)]}{s - s_V + i\epsilon}, \quad (21)$$

with s_{th} the corresponding vector meson threshold for the decay channels with the ρ or \bar{K}^* mesons. Therefore, the convolution of the $G_k(s)$ loop function defined in Eq. (18) with the

vector meson spectral function given by Eq. (21) provides

$$G(\sqrt{s}, M_k, m_k) = \frac{\int_{(M_V-2\Gamma_V)^2}^{(M_V+2\Gamma_V)^2} ds_V G(\sqrt{s}, \sqrt{s_V}, m_k) \times \text{Im}[D(s_V)]}{\int_{(M_V-2\Gamma_V)^2}^{(M_V+2\Gamma_V)^2} ds_V \text{Im}[D(s_V)]}, \quad (22)$$

where the limits $(M_V \pm 2\Gamma_V)^2$ are considered to be a reasonable cut in the integration above. These cuts cause a small deviation of the normalization of the Breit-Wigner distribution encoded in the spectral function in Eq. (20) and in order to reestablish it we divided by the integral defined in the denominator in Eq. (22).

By looking for poles of Eq. (17) in unphysical Riemann sheets of the complex \sqrt{s} variable, two poles can be found in the $I = 1/2$ channel, a broader one at $\sqrt{s_p} = (1195 - i123)$ MeV and a narrower one, at $\sqrt{s_p} = (1284 - i73)$, where, for poles not very far from the real axis, $\sqrt{s_p}$ can be approximated by $\sqrt{s_p} = (M_p - i\Gamma/2)$ in which the real part stands for the pole mass whereas the imaginary one is associated with half the width. For a matter of convenience we shall refer to the former as pole *A* and *B* for the latter one. For completeness we show in Table I the parameters obtained in Ref. [8] for the numerical calculation of Eq. (17) described in this section, and the couplings to the resonances obtained for each channel.

TABLE I. Parameters used in Ref. [8]. In the first line: values for the subtraction constant α , the scale of dimensional regularization μ along with the two K_1 poles are given. On the lower part: the channels and their corresponding couplings $g_i^{A(B)}$ to each K_1 pole *A* and *B*.

$\alpha(\mu)$ sub. constant	μ scale	Lower pole (A)	Higher pole (B)
-1.85	900	(1195 - i123) MeV	(1284 - i73) MeV
Channels		Couplings g_i^A	g_i^B
$\phi \bar{K}$		$2096 - i1208$	$1166 - i774$
$\omega \bar{K}$		$-2046 + i821$	$-1051 + i620$
$\rho \bar{K}$		$-1671 + i1599$	$4804 + i395$
$\bar{K}^* \pi$		$4747 - i2874$	$769 - i1171$

In Table I we also show the couplings for the i -th channel $g_i^{A(B)}$ to each $K_1(1270)$ pole.

This will be important in order to study the behavior of the distributions given in Eq. (11) considering each pole contribution individually. The amplitudes given in Eq. (17) contain the information about the whole dynamics for the PV interaction, including the resonance structure, and not only the resonances themselves. Although both poles are intertwined in the amplitude of Eq. (17), it is also interesting for illustrative purposes to differentiate the contribution from each individual pole. Since it is not possible to isolate directly each pole contribution from Eq. (17), this task can be achieved by adopting a Breit-Wigner shape for those amplitudes. Then, at the pole position, we have

$$t_{i,j}^{IA(B)} = \frac{g_i^{A(B)} g_j^{A(B)}}{s - s_p}, \quad (23)$$

with s_p the pole position of the K_1 poles A and B whereas $g_{i(j)}^{A(B)}$ stands for the coupling of the $i(j)$ -th channel to the pole $A(B)$. We know that the closer to the real axis these poles are the better this approximation works. In addition, it is expected that experimentally these amplitudes are parametrized by a Breit-Wigner form so that, by adopting it in our formalism, a comparison between our results and those from future experiments is more reasonable. Furthermore, this parametrization can also be used to encode the double-pole K_1 structure if we assume that the amplitudes are given by a double-Breit-Wigner shape defined as

$$T_{i,j} = t_{i,j}^{IA} + t_{i,j}^{IB}, \quad (24)$$

where $t_{i,j}^{IA}$ and $t_{i,j}^{IB}$ are given by Eq. (23) for poles A and B , respectively.

III. RESULTS

The values for the two $K_1(1270)$ poles along with their coupling constants to each channel under consideration are given in Table I, which were taken from Tables III and IV in Ref. [8].

As explained in the previous section, we have implemented a convolution with the vector meson spectral function in order to take into account the finite widths of the ρ and \bar{K}^* mesons. As a consequence, the phase space for both $\bar{B}^0 \rightarrow J/\psi \rho^+ K^-$ and $\bar{B}^0 \rightarrow J/\psi K^{*-} \pi^+$ decays get nonzero values below the corresponding PV threshold. This effect is specially relevant for the $\rho \bar{K}$ channel. Furthermore, in Eqs. (15) and (16) there is a global normalization factor by virtue of the weak vertex in Fig. 1. This global factor is the same for both decays we are concerned with, and it does not play a relevant role in our results since what

matters is the relative strengths between the different mass distribution evaluated for each mechanism we are considering and their shapes. Actually, this global normalization, C , is the only free parameter in our model.

We should note that the Chiral Unitary approach applied in this case has a range of applicability up to about 1500–1600 MeV in the invariant masses. We plot the distributions in the whole range but one should not pay much attention to the predictions for the high invariant masses.

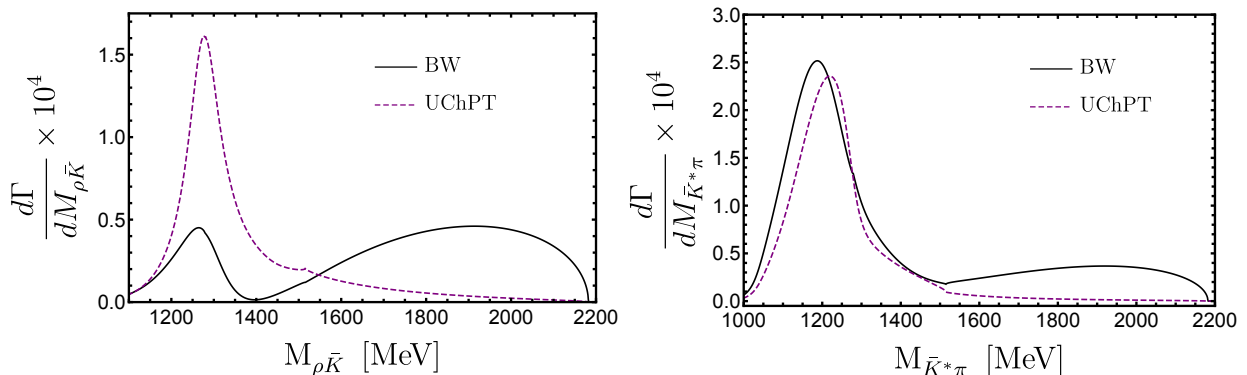


FIG. 4. a) $d\Gamma/M_{\rho\bar{K}}$ invariant mass distribution for $\bar{B}^0 \rightarrow J/\psi \rho \bar{K}$ and b) $d\Gamma/M_{\bar{K}^*\pi}$ distribution for $\bar{B}^0 \rightarrow J/\psi \bar{K}^* \pi$ reactions.

In Fig. 4 we show the PV invariant mass distribution for $\bar{B}^0 \rightarrow J/\psi \rho^+ K^-$ (left panel) and $\bar{B}^0 \rightarrow J/\psi K^{*-} \pi^+$ (right panel) reactions. In each case, the dashed lines are the results obtained using the unitarized amplitudes for the two-body PV final state interaction, Eq. (17), according to the Chiral Unitary approach [15–17], labeled as UChPT. On the other hand, the solid lines are the curves obtained if we parametrize the two-body PV amplitudes in Eq. (17) by using a double Breit-Wigner-like shape, as defined in Eq. (24). Both pseudoscalar-vector meson spectra manifest the $K_1(1270)$ state contribution. In fact, as discussed previously, it was shown in Ref. [8] that this state has a double-pole hadronic structure, which is dynamically generated via PV final state interaction in coupled channels. Therefore, we expect that this double-pole resonance influence the PV mass distribution shape since the final state interaction mechanism that generates those poles is encoded in the scattering amplitudes of Eq. (17) that enters in $d\Gamma/dM_{\rho\bar{K}}$ and $d\Gamma/dM_{\bar{K}^*\pi}$ through Eqs. (15) and (16), respectively, or through Eq. (24) in case of using a parametrization as a double Breit-Wigner like shape.

A clear indication of the influence over these shapes comes into view by comparing the

energy region where both distribution peak, which are different. For the $\rho^+ K^-$ case (left panel), the mass distribution has a pronounced peak at 1284 MeV right at the energy region where the highest $K_1(1270)$ mass pole emerges, *i. e.* the pole B in Table I. On the other hand, the $K^{*-}\pi^+$ distribution (right panel) has a peak at 1185 MeV, which is the energy region dominated by the lowest K_1 pole (pole A in Table I). Another evidence for the $K_1(1270)$ manifestation in those distributions is that the former mass spectrum is narrower than the latter one. This must be the case since the highest mass pole is the narrower one and, according to our previous discussion, it should dominate the $\rho^+ K^-$ distribution. By contrast, the pole A , with width equal to 246 MeV, is broader than the pole B , with width around 176 MeV and, then the distribution where that former mass pole dominates must exhibit a broad shape, which is the feature we observe in the $K^{*-}\pi^+$ mass spectrum (right panel in Fig. 4).

The double Breit-Wigner-like shape, Eq. (24), is proportional to the effective couplings of the poles to the corresponding PV channels. By looking at Table I we see that the pole A couples more to the $\bar{K}^*\pi$ channel, unlike the highest one which couples more to the $\rho\bar{K}$ channel. Therefore, we should expect that the pole A dominates the $K^{*-}\pi^+$ spectrum whereas the highest prevails in the $\rho^+ K^-$ distribution. Note that this is exactly the behavior we notice in the results in Fig. 4.

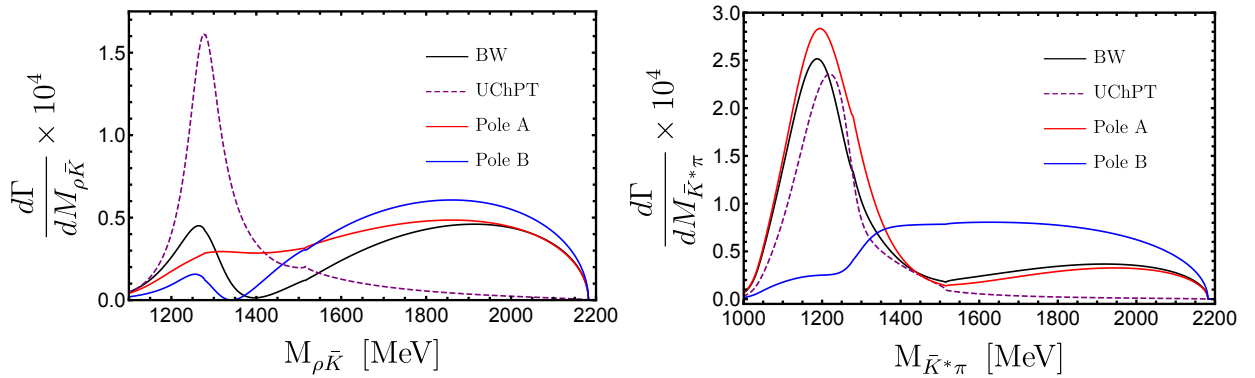


FIG. 5. a) $d\Gamma/M_{\rho\bar{K}}$ invariant mass distribution for the $\bar{B} \rightarrow J/\psi \rho \bar{K}$ reaction, as given in Fig. 4 (black solid line), compared with the curves obtained by considering only: pole A (red solid line), and pole B (blue solid line); b) $d\Gamma/M_{\bar{K}^*\pi}$ distribution for $\bar{B} \rightarrow J/\psi \bar{K}^* \pi$ channel also compared with distributions due to each pole contribution separately.

Next, we shall compare the results using the double-pole Breit-Wigner-like shape,

Eq. (24), and using the unitarized amplitudes, Eq. (17), with those considering just the pole A and the pole B contributions separately. This comparison is illustrated in Fig. 5 for both PV spectra. For the $\rho^+ K^-$ case, we observe that the total Breit-Wigner-like shape and Pole B curves have similar shapes in the energy region \sqrt{s} where that K_1 mass pole peaks. Likewise, the same behavior is seen in the $K^{*-}\pi^+$ case, but now with the corresponding Breit-Wigner-like curve showing its maximum exactly at the energy region where the K_1 lowest pole peaks. The UChPT results also follow the same pattern, *i. e.* the maxima for the bumps are located at the corresponding \sqrt{s} in which the poles A and B manifest themselves, respectively, in the $\bar{K}^*\pi$ and $\rho\bar{K}$ spectra.

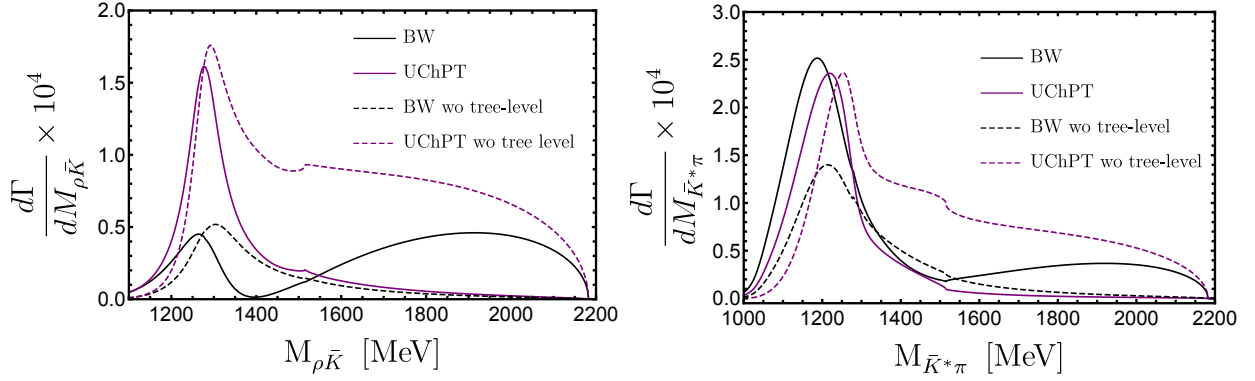


FIG. 6. a) $M_{\rho\bar{K}}$ invariant mass distribution for $\bar{B} \rightarrow J/\psi \rho \bar{K}$ reaction with and without the tree-level mechanism; b) $M_{\bar{K}^*\pi}$ distribution for $\bar{B} \rightarrow J/\psi \bar{K}^* \pi$ channel also compared with distribution without no interference between tree-level and the resonant part of the amplitude.

It is worth emphasizing the major role played by the FSI (implemented here by using the ChUPT) on the shapes of the spectra. Indeed, the main contribution for the distributions is solely due to the resonant part in the mechanism illustrated in Fig. 3 by the loops by means of which the two $K_1(1270)$ poles come into play. To show this we turn off the tree level mechanism in Fig. 3. By doing so we are eliminating the interference effects on the $d\Gamma/dM_{\rho\bar{K}}$ and $d\Gamma/dM_{\bar{K}^*\pi}$ distribution shapes and we are just left with the resonant contribution giving rise to the two $K_1(1270)$ poles. In Fig. 6 we confront the results obtained considering only the resonant part (dashed lines) with those for the whole mechanism: tree-level + resonant parts (solid lines). Notice that for the $\bar{K}^*\pi$ channel the shapes of the UChPT curves with and without the tree-level contributions are similar, which indicate that the tree-level plays a minor role on them, causing only a small difference between the location of the bumps.

Incidentally, the same behavior happens for the results for the double-pole Breit-Wigner like shape parametrization labeled as Total. In this case, the effect of turning off the tree-level contribution is more visible in the strengths of the spectra than shifting the curves. It decreases the maximum strength of the peak by half of its value. Nonetheless, the locations of those peaks are nearly the same. For the $\rho\bar{K}$ channel we also observe the same pattern, but the UChPT curves exhibit a noticeable difference in their shapes, with the one without the tree-level contribution distorted at the high energy range. Notwithstanding, by looking at both distributions it is clear that the tree-level contribution causes just a small shift of the curves, as it is evidenced by looking at both panels in Fig. 6. In other words, the resonant part mechanism prevails over the non-resonant one.

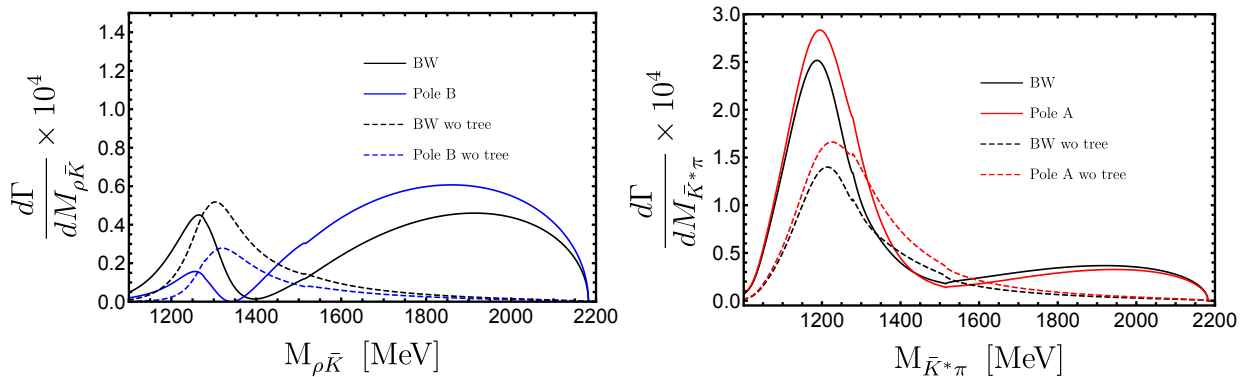


FIG. 7. a) $M_{\rho\bar{K}}$ invariant mass distributions for $\bar{B} \rightarrow J/\psi\rho\bar{K}$ reaction considering the following cases: whole mechanism and the pole A contributions with and without tree-level contributions (solid and dashed lines, respectively); b) $M_{\bar{K}^*\pi}$ distributions for $\bar{B} \rightarrow J/\psi\bar{K}^*\pi$ channel also compared with distribution without no interference between tree-level and resonant part of the amplitude (dashed lines).

As we have shown, each pole dominates the distribution for the channel to which they couple most. Then, any change in the distribution is a consequence of a change in these poles as the tree-level contribution is turned off. In Fig. 7 we show the results using Eq. (24) to parametrize the two-body amplitudes as well as the results regarding just the single-pole A or B (depending on which one couples mostly to the channel we are analyzing) in two scenarios: with and without the tree-level mechanism. The solid line curves correspond to the distributions with the whole mechanism of Fig. 3 included, that is, tree-level + resonance, while the dashed lines are the curves for the distributions with only the resonant mechanism

included, that is, without the tree-level contribution. For the $\rho\bar{K}$ case (left panel), we note that as the tree-level is turned off, the distribution corresponding to the double-pole Breit-Wigner parametrization is slightly shifted to the right. Nonetheless, the change caused by the inclusion of the tree-level mechanism is not enough to significantly distort the shape beyond the uncertainties.

Furthermore, by looking at the $\bar{K}^*\pi$ case (right panel) we see that the effect caused by the tree-level contribution is even smaller than in the previous case. The shapes for the curves obtained with and without including the tree-level mechanism are similar in both cases. The curve related to the double-pole Breit-Wigner parametrization (solid black line) and its counterpart without the tree-level (dashed black line) have similar shapes, with a small difference at the position for their respective peaks. The noticeable change is in the strength, which falls off by half, as could be already expected since this change is reflected in the behavior we noticed in the right panel in Fig. 6. The same behavior can be observed by comparing the results for the single-pole parametrization, pole A in this case. It is clear that the pole A is not altered much due to the inclusion of the tree-level mechanism. In other words, it is evident that the source of these changes in those distributions, even being such a small one, happens by a clear influence of the $K_1(1270)$ mass poles, reinforcing the important role played by its double-pole nature in those invariant mass distributions.

IV. CONCLUSIONS

We have theoretically investigated the double-pole structure of the $K_1(1270)$ resonance, which was shown in Ref. [8] to be dynamically generated through the pseudoscalar-vector meson interaction in coupled channels, by looking at the invariant mass distributions for the $\rho\bar{K}$ and $\bar{K}^*\pi$ pairs, respectively, in the $\bar{B} \rightarrow J/\psi\rho\bar{K}$ and $\bar{B} \rightarrow J/\psi\bar{K}^*\pi$ reactions. The final state interaction mechanism was implemented employing the Chiral Unitary approach in which the pseudoscalar-vector meson interaction gives rise to the two $K_1(1270)$ poles that, in our model, affect both the $\rho\bar{K}$ and $\bar{K}^*\pi$ distributions differently, a feature that allows us to unveil this double-pole structure in those reactions. This happens due to the relative weights between the different PV final states produced at tree level and, as a consequence of the implementation of the final state interaction, the distributions exhibit different shapes influenced by the two $K_1(1270)$ poles.

In particular, we have shown for the $\rho\bar{K}$ distribution associated with the $\bar{B} \rightarrow J/\psi\rho\bar{K}$ reaction that its shape is dominated by the contribution from the K_1 highest mass pole, whereas the lowest mass one contributes more for the $\bar{K}^*\pi$ distribution in the $\bar{B} \rightarrow J/\psi\bar{K}^*\pi$ decay. As we have pointed out, this comes about due to the coupling constants of those poles to the different channels considered in this work, more specifically, the $\rho\bar{K}$ and $\bar{K}^*\pi$ channels. On the other hand, it is important to stress that even though being possible to see one pole dominance over the other in each distribution, both PV spectra still have the two $K_1(1270)$ poles contributing to their shapes. In view of that, we also have modeled the two-body dynamics by using a double-pole Breit-Wigner like curve such that the contributions of the two poles could be disentangled. In this case, it is expected to observe the manifestation of each pole separately in the PV spectra to which they couple most. Apart from that we also have interference effects between the mechanisms illustrated in Fig. 3 such that the shapes do not correspond to a pure resonance manifestation. However, we have also shown how each spectrum responds to each pure resonant contribution: by modifying the location and shapes of the spectra, with the bumps corresponding to each pole in the energy range where those poles manifest, indicating the dominance of one pole over the other in the channels we are concerned with.

We end by noting that an experimental investigation of those reactions is important to shed light on the $K_1(1270)$ nature and also to provide a test for the Chiral Unitary approach employed in this work, implementing QCD dynamics at low energies, which has been an important theoretical tool to understand hadronic interactions, helping interpret many experimental reactions produced in present facilities, and making predictions to be tested in the future.

ACKNOWLEDGMENTS

This work is partly supported by the Spanish Ministerio de Economía y Competitividad and European FEDER funds under Contracts No. FIS2017-84038-C2-1-P B and No. FIS2017-84038-C2-2-P B. This project has received funding from the European Union's Horizon 2020 research and innovation programme under grant agreement No. 824093 for the STRONG-2020 project.

-
- [1] G. W. Brandenburg, *et al.* Phys. Rev. Lett. **36**, 703 (1976)
 - [2] C. Daum *et al.* [ACCMOR], Nucl. Phys. B **187**, 1-41 (1981)
 - [3] P. A. Zyla *et al.* [Particle Data Group], PTEP **2020** 8, 083C01 (2020)
 - [4] M. Suzuki, Phys. Rev. D **47**, 1252-1255 (1993)
 - [5] A. Tayduganov, E. Kou and A. Le Yaouanc, Phys. Rev. D **85**, 074011 (2012)
 - [6] Z. Q. Zhang, H. Guo and S. Y. Wang, Eur. Phys. J. C **78**, 219 (2018)
 - [7] L. Roca, E. Oset and J. Singh, Phys. Rev. D **72**, 014002 (2005)
 - [8] L. S. Geng, E. Oset, L. Roca and J. A. Oller, Phys. Rev. D **75**, 014017 (2007)
 - [9] G. Y. Wang, L. Roca and E. Oset, Phys. Rev. D **100**, 074018 (2019)
 - [10] G. Y. Wang, L. Roca, E. Wang, W. H. Liang and E. Oset, Eur. Phys. J. C **80**, 388 (2020)
 - [11] L. Micu, Nucl. Phys. B 10, 521-526 (1969).
 - [12] A. L. Yaouanc, L. Oliver, O. Pene, J. C. Raynal, Phys. Rev. D 8, 2223-2234 (1973).
 - [13] E. Santopinto, R. Bijker, Pys. Rev. C 82, 062202 (2010).
 - [14] A. Bramon, A. Grau, and G. Pancheri, Phys. Lett. B 283, 416 (1992).
 - [15] J. A. Oller, E. Oset, and J. R. Pelaez, Phys. Rev. Lett. 80, 3452 (1998).
 - [16] J. A. Oller, E. Oset, and A. Ramos, Prog. Part. Nucl. Phys. 45, 157 (2000).
 - [17] J. A. Oller, E. Oset, and J. R. Pelaez, Phys. Rev. D 59, 074001 (1999); Phy. Rev. D 60, 099906 (1999) (Erratum); Phy. Rev. D 75, 099903 (2007).